THE JOURNAL OF PHYSICAL CHEMISTRY Letters

pubs.acs.org/JPCL Letter

Edge Influence on Charge Carrier Localization and Lifetime in $CH_3NH_3PbBr_3$ Perovskite: *Ab Initio* Quantum Dynamics Simulation

Ran Shi, Andrey S. Vasenko, Run Long,* and Oleg V. Prezhdo

Cite This: *J. Phys. Chem. Lett.* 2020, 11, 9100–9109 Read Online

ACCESS | Metrics & More | Article Recommendations | Supporting Information

ABSTRACT: The distribution of charge carriers in metal halide perovskites draws strong interest from the solar cell community, with experiments demonstrating that edges of various microstructures can improve material performance. This is rather surprising because edges and grain boundaries are often viewed as the main source of charge traps. We demonstrate by *ab initio* quantum dynamics simulations that edges of the $CH_3NH_3PbBr_3$ perovskite create shallow trap states that mix well with the valence and conduction bands of the bulk and therefore support mobile charge carriers. Charges are steered to the edges energetically, facilitating dissociation of photogenerated excitons into free carriers. The edge-driven charge separation extends carrier lifetimes because of decreased overlap of the electron and hole wave functions, which leads to reduction of the nonadiabatic coupling responsible for nonradiative electron–hole recombination. Reduction of spatial symmetry near the edges activates additional vibrational modes that accelerate coherence loss within the electronic subsystem, further extending carrier lifetimes. Enhanced atomic motions at edges increase fluctuations of edge energy levels, enhancing mixing with band states and improving charge mobility. The simulations contribute to the atomistic understanding of the unusual properties of metal halide perovskites, generating the fundamental knowledge needed to design high-performance optoelectronic devices.

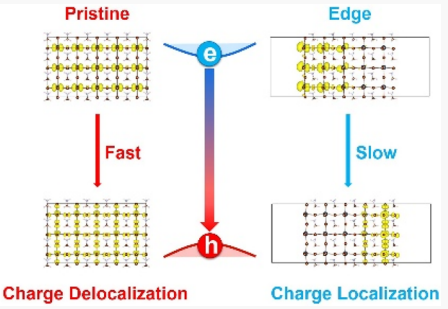

Hybrid organic–inorganic halide perovskites (HOIPs), such as $CH_3NH_3PbX_3$ [X = Cl, Br, I], are presently the focus of intense research directed toward their extremely fast progress in solar cell applications, with the record power conversion efficiency growing from 3.8%[1] in 2009 to the current maximum of 25.2%.[2] The superior optoelectronic properties of HOIPs, such as high absorption in the visible spectrum,[3] large charge carrier mobility[4] and diffusion length,[5] favorable defect tolerance,[6,7] efficient band gap tunability,[8,9] and long excited-state lifetime,[9,10] lay the foundation for multiple applications beyond photovoltaics[11,12] and including lasers,[13] field effect transistors,[14] photodetectors,[15] light-emitting diodes,[16] etc.

The carrier recombination time plays a pivotal role in the design of HOIP solar cells. It is used to estimate the perovskite film quality, with longer decay time implying better performance and higher device efficiency.[17] Nonradiative electron–hole recombination constitutes the main pathway for charge and energy losses in perovskite solar cells. Importantly, there exist drastic performance variations among different areas of even a single perovskite microstructure.[17−19] Rational device design requires a clear understanding of the connection between the local material morphology, e.g., bulk versus edges, and photo-electric properties, as can be deduced from excited-state dynamics studies. The lack of fundamental understanding of the excited-state dynamics gives rise to debates regarding the nature of photo-excited species, whether they are neutral excitons, free charge carriers, or their mixture or even more complex species such as trions and multiple excitons.[18,20−23] As demonstrated by the Ginger research group in 2015, librational motions of the $CH_3NH_3^+$ (MA^+) cations modulate the electrostatic potential and suppress exciton formation, such that there exists no excitonic transitions in the edge structures, where the photo-induced dynamics is governed solely by uncorrelated free charge carriers.[17]

The heterogeneous local variation of photoluminescence (PL) yield and lifetime in different parts of a crystal structure is a controversial subject in the past few years.[18,20,21,24−28] In 2015, Grancini and co-workers suggested using the micro-PL spectroscopy that edge surfaces exhibited faster carrier recombination dynamics with respect to the central region of $MAPbI_3$ perovskite single crystals because of surface reconstruction and associated structural changes.[20,28] In contrast, Chen et al. and Harel et al. obtained subsequently the opposite evidence of slower PL decay near crystal edges, as compared with the crystal internal region, according to the spatially resolved experimental studies.[24,25] In addition, edge-

Received: September 13, 2020
Accepted: October 5, 2020
Published: October 13, 2020

https://dx.doi.org/10.1021/acs.jpclett.0c02800
J. Phys. Chem. Lett. 2020, 11, 9100–9109

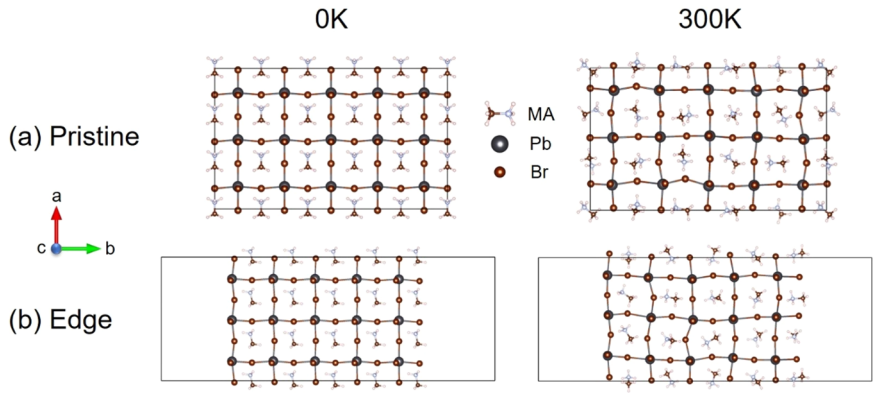

Figure 1. Optimized geometry (0 K) and a representative snapshot from the MD trajectory (300 K) of (a) pristine and (b) edge $MAPbBr_3$. The structures at 0 and 300 K demonstrate the importance of thermal atomic fluctuations that influence electron−phonon interactions. The fluctuations are stronger in the edge configuration (Table 1).

assisted exciton dissociation and generation of long-lived charge carriers for low-dimensional halide perovskites was demonstrated by both experiment[29,30] and atomistic simulations.[31,32] Recently, the edge effects in single-crystal $MAPbBr_3$ perovskites were investigated by Zhang et al.,[26] who proposed that fluctuations of the electrostatic potential near the edges could accelerate electron−hole separation leading to formation of free charge carriers rather than bounded excitons, and thus resulting in long excited-state lifetimes. However, the atomistic mechanisms of the influence of the edge structures on the nonradiative charge recombination are still missing, while their understanding is of utmost importance for material processing and device optimization.

In this Letter, we use real-time time-dependent density functional theory (TDDFT)[33] and nonadiabatic (NA) molecular dynamics (MD)[34−36] to simulate directly the charge carrier recombination dynamics in the $MAPbBr_3$ perovskite with and without edges. The simulations establish the exciton dissociation mechanism and the origin of the improved excited-state properties. Edge structures with unsaturated chemical bonds create states that are energetically close (∼0.1 eV) to valence and conduction bands and that mix well with the band states. The edge states provide a driving force for separation of photo-generated excitons into free electrons and holes. At the same time, the electrons and holes are coupled to the bands and remain mobile. Enhanced atomic motions at edges increase fluctuations of edge-state energies, facilitating coupling of edge and bulk states. The decreased overlap between electron and hole wave functions in the presence of edges reduces the NA coupling and slows down the nonradiative charge recombination. Symmetry breaking and enhanced atomic fluctuations at the edges activate additional vibrational modes that couple to the electronic subsystem and accelerate loss of quantum coherence, further extending carrier lifetimes. The theoretical analysis provides a fundamental understanding of the relationships between local morphology and photo-physical properties of metal halide perovskites, highlighting their unique structural and electronic properties and assisting in the design of high-efficiency solar cells and related devices.

This NAMD[34−36] simulations have been carried out with the decoherence-induced surface hopping (DISH)[37] algorithm based on a classical path approximation, implemented within the time-dependent Kohn−Sham (KS) theory.[38] The lighter and faster electrons are treated quantum mechanically, whereas the heavier and slower nuclei are handled semiclassically.[36,39] Decoherence, driven by coupling of the electronic system to atomic motions, destroys superposition formed between pairs of electronic states due to NA coupling and leads to branching of nuclear trajectories.[37,40] The decoherence time is estimated as the pure-dephasing time in the optical-response theory.[41] Decoherence effects are needed because the decoherence time is significantly shorter than the nonradiative electron−hole recombination time.[42,43] The method has been applied successfully to investigate photoexcitation dynamics in a broad range of condensed-phase materials, including perovskites containing grain boundaries,[44] chemical dopants,[45] defects,[46] and water molecules;[46] low-dimensional Ruddlesden−Popper and Dion−Jacobson perovskites;[47,48] semiconducting[49−51] and metallic nanoparticles;[52,53] black phosphorus;[54,55] and so on.[56−63]

The Vienna *ab initio* simulation package (VASP)[64] has been employed to perform geometry optimization, adiabatic MD simulations, and electronic structure and NA coupling calculations. The exchange−correlation interactions are described by the Perdew−Burke−Ernzerhof (PBE) functional,[65] while the interactions between ionic cores and valence electrons are treated with the projector-augmented wave (PAW) approach.[66] The plane wave energy cutoff has been set to 400 eV. Atomic coordinates are relaxed with a $2 \times 1 \times 6$ Monkhorst−Pack k-point mesh,[67] and much denser $6 \times 4 \times 8$ and $6 \times 1 \times 8$ k-meshes have been used for electronic structure calculations of the pristine and edge $MAPbBr_3$ perovskite systems, respectively. The adiabatic MD and NAMD simulations have been performed at the R-point, which contains the direct band gap of the $MAPbBr_3$ perovskite simulation cell under investigation. Geometry optimization has been stopped when the ion forces have become less than 10^{-3} eV·Å^{-1}. The Grimme DFT-D3 method with the Becke−Johnson damping is used to describe the van der Waals interactions.[68,69] After geometry optimization corresponding to 0 K, the systems have been heated to 300 K with repeated velocity rescaling for 2 ps. Then, 6 ps adiabatic MD trajectories have been generated in the microcanonical ensemble with a 1 fs atomic time step, and the NA couplings between the conduction band minimum (CBM) and valence band maximum (VBM) have been computed along these trajectories. The 6 ps of NA coupling and orbital energies have been repeated multiple times and used to perform longer-time NAMD calculations.[34−36] 2000 initial geometries have

https://dx.doi.org/10.1021/acs.jpclett.0c02800
J. Phys. Chem. Lett. 2020, 11, 9100−9109

been selected randomly from the 6 ps of the NA Hamiltonian, and 100 realizations of the DISH stochastic process have been sampled for each initial geometry using the PYXAID code.[34,35]

Both pristine and edge simulation cells contain 180 atoms. The pristine simulation cell is modeled by a $3 \times 5 \times 1$ supercell in cubic phase, whose optimized lattice parameter of the unit cell is 5.928 Å, agreeing well with the experimental value of 5.938 Å.[70] The edge simulation cell is constructed by cutting the three-dimensional periodic system along the *b*-axis and adding 20 Å of vacuum so that spurious interactions between the two edges are removed. This setup has proven to provide an effective description of stoichiometric perovskite edges according to our group's previous work on the $(BA)_2PbI_4$ 2D perovskite.[31]

The edges of the $MAPbBr_3$ perovskite may be terminated in three different ways. A stoichiometric structure necessitates that the two edges are terminated asymmetrically, with MAI and PbI_2 on the different sides. Alternatively, one can consider nonstoichiometric systems with symmetric termination of the edges with either MAI or PbI_2 on both sides. Our main simulation is carried out with the stoichiometric structure, as shown in Figure 1. The other two nonstoichiometric MAI-terminated and PbI_2-terminated structures display similar properties, as shown in Figure S1 of the Supporting Information. In order to mimic the experimental viewpoint regarding electrostatic potential fluctuations caused by MA librations at edges,[26] we rotate the MA cations to different angles, as highlighted by the red boxes in Figure S2.

Figure 1 shows the optimized geometries at 0 K and representative snapshots from the MD trajectories at 300 K for pristine and edge $MAPbBr_3$. Thermal fluctuations of the inorganic Pb−Br lattice may influence electron−hole interactions, because Pb and Br atoms determine the fundamental band gap in the $MAPbBr_3$ perovskite. The calculated average Pb−Br bond length is 2.981 Å at 0 K in the optimized pristine structure, agreeing with the previous calculations and the experimental values.[71,72] Under thermal fluctuations, the canonically averaged Pb−Br bond length in the pristine system increases slightly to 2.986 Å at 300 K, a 0.005 Å extension. A strong periodic order and a rigid inorganic framework are maintained. In comparison, the edge system undergoes a notably larger deformation due to thermal motions. The Pb−Br bond extends by 0.026 Å on average, from 2.987 Å at 0 K to 3.013 Å at 300 K. The edge structure undergoes significant local distortions due to thermal fluctuations, and such distortions influence electron−vibrational interactions and electron−hole recombination.

Additional information about the thermal atomic fluctuations in the pristine and edge structures is provided by the canonically averaged standard deviations of the positions for each type of atom, $\sigma_i = \sqrt{(\langle \vec{r}_i - \vec{r}_i \rangle)^2}$. Here, $\vec{r}_i$ represents the location of atom *i*, and the angular bracket stands for canonical averaging. The calculations are done separately for the MA, Pb, and Br atoms (Table 1). The atomic fluctuations are consistently larger for edge than pristine $MAPbBr_3$. The increase is more significant for the Pb and Br atoms of the inorganic lattice, compared to the organic MA cations, indicating that the structural integrity of the inorganic lattice is notably undermined at the edges.

Table 1. Standard Deviations (Å) in the Positions of MA, Pb, and Br Atoms in Pristine and Edge $MAPbBr_3$ at 300 K

	MA	Pb	Br
pristine	0.698	0.468	0.627
edge	0.776	0.672	0.745

Generally, strong atomic fluctuations can create disorder that localizes electron and hole wave functions and decreases electron−hole interactions and the NA coupling. At the same time, larger atomic fluctuations lead to anharmonicities that can allow a broader range of phonon modes to couple to the electronic system. This can both increase the NA coupling and shorten the coherence time. A decreased electron−hole overlap and shortened coherence time extend the excited-state lifetime, while an increased NA coupling decreases the lifetime.

The projected density of states (PDOS) of the pristine and edge structures computed using the optimized geometries are presented in Figure 2, showing contributions from the s and p_x, p_y, p_z orbitals of the Pb and Br atoms. For the pristine $MAPbBr_3$, the VBM arises from the Pb (6s)−Br (4p) antibonding interaction. The CBM originates from interaction of Pb (6p) and Br (4p) orbitals. The Pb (6p) orbitals contribute most to the CBM. The organic MA cations contribute to neither the CBM nor the VBM. Because the nonradiative electron−hole recombination takes place between the CBM and the VBM, the NA coupling is generated by the Pb and Br atoms. The organic MA cations can contribute to the NA coupling indirectly, by perturbing motions of the inorganic Pb−Br sublattice and by electrostatic interaction with the charges. The calculated direct band gap for pristine $MAPbBr_3$ is 1.94 eV at the R-point, in agreement with the previous DFT calculations with the PBE functional.[73] The gap is underestimated by 0.41 eV relative to the experimental value of 2.35 eV.[74,75] In order to account for the difference, we scale the calculated band gaps in both pristine and edge systems by adding 0.41 eV during the NAMD calculations. Exposure to a vacuum layer narrows the VBM−CBM energy gap to 1.76 eV in the edge structure, because unsaturated chemical bonds induce shallow defect states near the band edges. These states mix well the band states of the bulk and extend relatively deep inside the slab.

In general, a smaller band gap favors a greater NA coupling and a faster nonradiative recombination. However, surprisingly, this is not the case in the present system. The edge states promote charge localization and exciton dissociation, separating electrons and holes, decreasing overlap of the electron and hole wave functions, and extending the excited-state lifetime. It is essential that the edge states do not create deep traps inside the band gap and that they couple well and mix with the states of the conduction and valence bands. These properties ensure that the charges are not permanently trapped at the edges and can travel and carry current to the electron and hole collection layers in a solar cell.

Figure 3 depicts the charge density distributions of the VBM and CBM in the two systems in their optimized geometries and for representative geometries at ambient temperature. The results agree with the PDOS analysis in Figure 2. The electrons are supported primarily by Pb atoms, while the holes distribute on both Br and Pb atoms. Apart from the band gap, charge carrier recombination is strongly influenced by the NA coupling, whose strength is determined by the overlap of the CBM and VBM wave functions, $\langle \phi_{CBM} | \nabla_R | \phi_{VBM} \rangle$. As demonstrated in Figure 3a for bulk pristine $MAPbBr_3$, electrons and holes are delocalized over the inorganic lattice

https://dx.doi.org/10.1021/acs.jpclett.0c02800
J. Phys. Chem. Lett. 2020, 11, 9100−9109

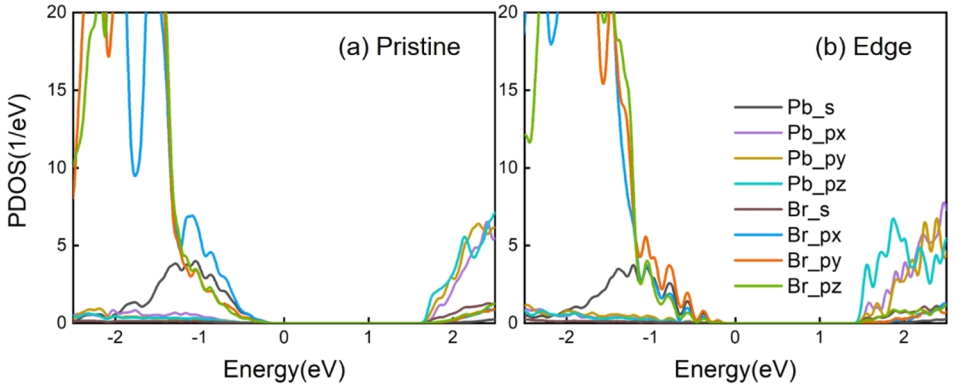

Figure 2. Projected density of states (PDOS) of (a) pristine and (b) edge $MAPbBr_3$ calculated with the optimized geometries and separated into contributions from Pb and Br atomic orbitals. The CBM is formed by Pb orbitals, while the VBM arises primarily from Br orbitals and secondarily from Pb orbitals. Zero energy is set to the Fermi level. The edge structure has a smaller band gap due to shallow edge defect states which mix well with band states.

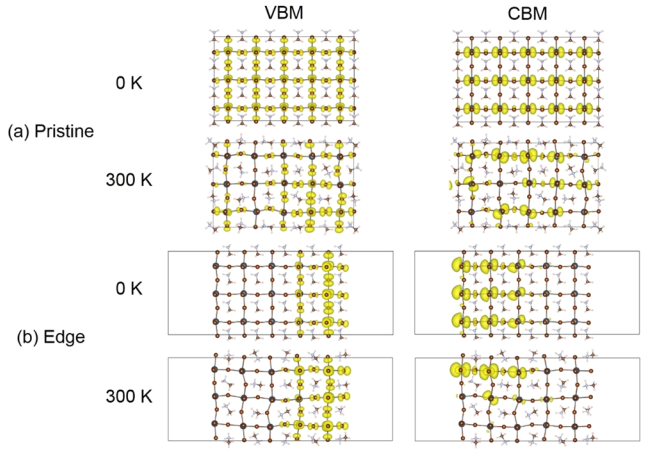

Figure 3. VBM and CBM charge densities in (a) pristine and (b) edge $MAPbBr_3$ in their optimized structures and for a representative geometry at room temperature. Thermal disorder enhances the localization. Larger orbital localization in the edge system leads to weaker NA coupling and slower nonradiative electron−hole recombination.

uniformly at 0 K. The electron and hole wave functions overlap well, favoring larger NA coupling. The VBM and CBM charge densities are localized near edges in the edge system at 0 K (Figure 3b). Moreover, the electrons and holes are located at the opposite edges. This factor facilitates exciton dissociation into free charge carriers and extends carrier lifetimes. One can attribute the opposite edge locations of the VBM and CBM to asymmetry of the termination of the simulation cell and the fact that electrons are supported by Pb atoms, while holes are primarily on Br atoms. In order to test this hypothesis, we performed additional calculations on systems with symmetric edge terminations (Figure S1). Here also, the VBM and CBM are localized on the opposite sides. We further tested the role of rotation of the MA cations, which can create long-range electrostatic fields separating electrons and holes. The VBM and CBM tend to localize on the opposite edges with MA rotation as well (Figure S2). It is possible that in some configurations the VBM and CBM are localized on the same edge and overlap. However, electrons and holes are supported by different atoms (Pb and Br) and are driven in opposite directions by electric fields present in the system. Further, localization of two particles at the same place is unlikely statistically because of decreased entropy. These three factors, i.e., localization of electrons and holes on different atoms, their opposite response to internal electric fields, and entropy, compete with electron−hole attraction, which is well-screened because of the material's large dielectric constant that increases further upon light irradiation.[76] Even if electrons and holes are located on the same edge of a crystal, it is unlikely that they are found at the same place. Importantly, experiments confirm that edges favor exciton dissociation.[26]

Thermal atomic fluctuations at ambient temperature intensify charge localization in both systems (Figure 3). Still, the electrons and holes are separated much more and the wave functions overlap much less in the edge system compared to the pristine system. Consequently, the average absolute NA coupling is nearly 4 times weaker in the edge system (0.17 meV) relative to the pristine system (0.61 meV) (Table 2).

Table 2. Band Gap, Average Absolute NA Coupling, Pure-Dephasing Time, and Nonradiative Electron−Hole Recombination Time for Pristine and Edge $MAPbBr_3$

	band gap (eV)	NA coupling (meV)	dephasing (fs)	recombination (ns)
pristine	2.35	0.61	4.3	0.77
edge	2.17	0.17	2.4	2.54

The decreased NA coupling in the presence of edges extends charge carrier lifetime. It is important to note that the two edges are close to each other in the simulated system because of computational limitations on the system size. In practice, edges are separated by large distances, and the NA coupling between edge separated electrons and holes is significantly smaller than in the present calculation.

The inverse participation ratio (IPR)[77,78] characterizes the degree of orbital localization. It is defined as

$$\mathrm{IPR} = N \cdot \frac{\sum k_i^4}{\left(\sum k_i^2\right)^2}$$

$$\mathrm{IPR} \in (0, 1]$$

where N is the number of grid points and k_i is the charge density within the volume corresponding to grid point i. The number of grid points is determined by the kinetic energy cutoff for the plane wave basis and is in the hundreds of

https://dx.doi.org/10.1021/acs.jpclett.0c02800
J. Phys. Chem. Lett. 2020, 11, 9100−9109

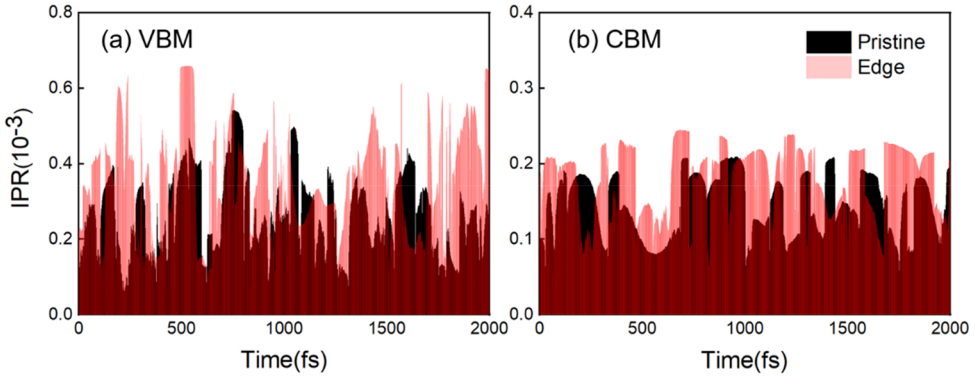

Figure 4. Evolution of the inverse participation ratio (IPR) of (a) VBM and (b) CBM for pristine and edge $MAPbBr_3$. The higher the IPR value, the stronger the localization of the charge density. Larger IRP in the edge system corresponds to reduced electron−hole overlap and smaller NA coupling (Table 2). The VBM is localized more than the CBM, because holes are supported primarily by nonmetal atoms (Br), while electrons are supported by metal atoms (Pb), and bonds involving metal atoms are less directional and more stable to perturbation.

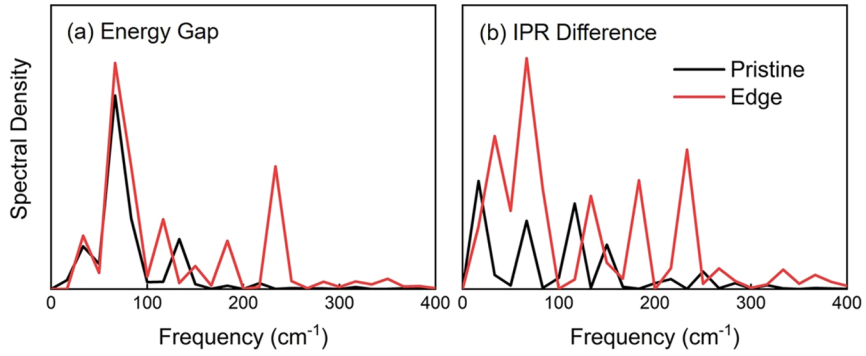

Figure 5. Spectral density obtained by FTs of the ACF for phonon-induced fluctuations in (a) VBM−CBM band gap and (b) VBM−CBM IPR difference in pristine and edge $MAPbBr_3$. The nonradiative electron−hole recombination is driven by low-frequency modes. The edge structure exhibits a broader range of frequencies due to symmetry breaking and relaxation of electron−phonon coupling selection rules.

thousands. The IPR value varies from 0 to 1, as follows from wave function normalization and mathematical properties of the above expression. The larger the IPR, the more highly localized the charge density. If an IPR equals 1, the charge is totally located on a single site.

Figure 4 presents the IPR for the VBM and CBM orbitals along 2 ps parts of the trajectories at 300 K for the pristine and edge systems. The IPR values are larger in the edge system, for both VBM and CBM, indicating more localized states, in agreement with the charge densities shown in Figures 3, S1, and S2. The canonically averaged IPR values are 3.61×10^{-4} versus 2.66×10^{-4} for the VBM and 1.82×10^{-4} versus 1.46×10^{-4} for the CBM, with the larger values corresponding to the edge system. Perhaps surprisingly, the difference of the averaged IPR between the edge and pristine systems is only a factor of 1.25−1.36, indicating that thermal fluctuations induce a significant amount of disorder to localize electrons and holes even in bulk $MAPbBr_3$. This observation also confirms that edge states mix well with band states. Interestingly, the localization is larger for the hole (VBM) than electron (CBM). This can be attributed to the fact that electrons are supported by metal atoms (Pb), while holes are localized primarily on nonmetal atoms (Br). Bonds involving nonmetals are more directional, and distortion of such bonds causes more significant charge localization, as observed in our previous simulations of semiconductor quantum dots[79,80] and 2D perovskites.[31] The larger charge localization in the edge structure corresponds to a smaller overlap of electron and hole wave functions, a weaker NA coupling, and a longer lifetime (Table 2).

Electron−vibrational interactions initiate inelastic and elastic electron−phonon scattering events, both of which exert influence on nonradiative electron−hole recombination. Inelastic scattering dissipates the electronic energy to phonons, while elastic scattering destroys the superposition formed between VBM and CBM via NA coupling, giving rise to quantum decoherence. Decoherence is closely related to pure-dephasing in the optical response theory.[41] It is typical that fast decoherence delays quantum dynamics. Quantum transitions can stop entirely if the decoherence time is infinitesimal, manifested by the quantum Zeno effect.[41,81]

For purpose of diagnosing the phonon modes participating in the nonradiative electron−hole recombination dynamics, we calculated spectral densities by performing Fourier transforms (FTs) of the autocorrelation functions (ACFs) for the phonon-induced fluctuations of the band gap and the difference of the IPRs of the CBM and VBM (Figure 5). According to both FTs, the electron−hole recombination dynamics is driven by low-frequency phonons with frequencies under 300 cm^{-1}. A wider spectrum of modes appears in the IPR FT, because it reflects properties of the wave functions rather than energy, and wave functions are more sensitive to perturbations. For instance, the first-order correction to the energy is zero in the mean-field theory, including DFT, while it is not zero for the wave function. The micro-Raman spectral measurements by Zhang et al.[26] can be used to assign the

https://dx.doi.org/10.1021/acs.jpclett.0c02800
J. Phys. Chem. Lett. 2020, 11, 9100−9109

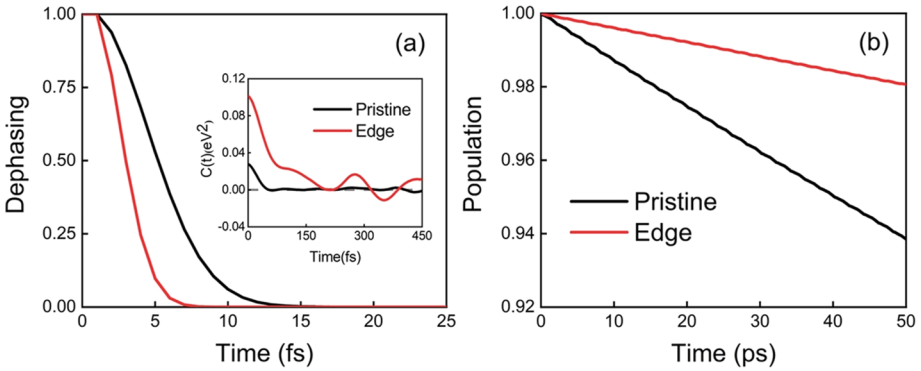

Figure 6. (a) Pure-dephasing functions for the CBM−VBM transition in the pristine and edge $MAPbBr_3$ systems. The inset shows the unnormalized ACFs. Larger initial values of the un-ACFs lead to faster pure-dephasing. (b) Nonradiative electron−hole recombination dynamics in pristine and edge $MAPbBr_3$. The edge structure exhibits slower decay because of smaller NA coupling and faster pure-dephasing (Table 2).

peaks. The dominant peak around 85 cm^{-1} can be assigned to the Pb−Br stretching mode, and the side peak at 60 cm^{-1} corresponds to the Br−Pb−Br bending vibration.[26,82−84] These modes couple most strongly to the recombining electrons and holes, because the band edge states are supported by the inorganic lattice. The minor peaks located at 120−180 cm^{-1} are due to the Raman active librations of the fast and light organic MA cations.[85] The signals in the 200−350 cm^{-1} range arise from MA torsional motions.[26,85] Even though the MA cations do not contribute to the electron and hole wave functions, their motions influence the electron−phonon interaction. MA motions can perturb the inorganic Pb−Br lattice sterically, and the asymmetric charge destribution of the MA cations leads to fluctuating electric fields interacting with the charge carriers.

Compared to the pristine structure, the edge shows higher peaks and a broader range of frequencies in Figure 5. Several higher-frequency motions arising from the MA cations are active in the edge system, while they are inactive in the pristine structure. This is because edges break the structural symmetry of the material, relaxing electron−phonon coupling selection rules. Larger amplitude motions of the MA dipoles, observed in the Raman experiments,[24,26] increase anharmonicity[86] that relax the coupling selection rules further. The conclusions apply to FTs of both band gap and IPR difference. Higher peak intensities and a broader range of phonon modes present in the edge system contribute to the more rapid coherence loss (Table 2).

We estimate the decoherence time as the pure-dephasing time of the optical response theory.[41] Under the second-order cumulant approximation, the pure-dephasing function, $D_{ij}(t) = \exp\left(-\frac{1}{\hbar^2}\int_0^t dt' \int_0^{t'} dt'' C_{ij}(t'')\right)$, is determined by the unnormalized ACF (un-ACF), $C_{ij}(t) = \langle \delta E_{ij}(t')\delta E_{ij}(t - t')\rangle_{t'}$, of the deviation, $\delta E_{ij}(t)$, of the band gap from its canonically averaged value. The pure-dephasing time is controlled by the rate of the un-ACF decay and its initial value. The larger the initial value and the faster the decay, the shorter the coherence time.[87]

Figure 6 displays the pure-dephasing functions and un-ACFs for the CBM−VBM transition in the pristine and edge systems. Fitting pure-dephasing functions to a Gaussian, $\exp(-0.5(t/\tau)^2)$, gives the pure-dephasing time, τ, shown in Table 2. The pure-dephasing times are sub-5 fs in both systems, because electrons and holes are localized on different atoms, and the fluctuations of the CBM and VBM energies are poorly correlated. The fluctuations of the CBM−VBM energy gap are large, because the material undergoes substantial distortions at ambient temperature, and electrons and holes become localized in different parts of the material because of thermally induced structural disorder. In addition, multiple phonon modes interact with the electronic subsystem, as demonstrated in Figure 5. The calculated pure-dephasing time is almost twice shorter for the edge than pristine system. As presented in the inset of Figure 6, the un-ACFs decay on similar time scales, and therefore, the pure-dephasing rates are determined by the un-ACF initial values, which are equal to the square of the energy gap fluctuation.[87] The un-ACF initial value is larger for the edge system, rationalizing the shorter pure-dephasing. The large band gap fluctuation and the shorter pure-dephasing time in the edge system agree with the higher intensity of the major peak and a broader range of phonon modes coupled to the electronic transition (Figure 5a). Generally, rapid loss of coherence suppresses charge recombination. Thus, the short decoherence time contributes to the long charge carrier lifetimes and high efficiency of metal halide perovskites. The decoherence is shorter for the edge system because electrons and holes are more separated and less correlated (Figures 3, S1, and S2).

Figure 6b describes evolution of the excited-state populations in the pristine and edge systems, representing nonradiative electron−hole recombination. Fitting the short-time linear approximation to the exponential function, $P(t) = \exp(-t/\tau) \approx 1 - t/\tau$, gives the nonradiative decay times, τ, shown in Table 2. The recombination times are on the order of a nanosecond, in agreement with the results of the time-resolved experiments.[26,88,89] The recombination is slower in the edge system, confirming the experimental observation that edges assist in exciton dissociation and extend carrier lifetimes.[26] The band gap, NA coupling, and pure-dephasing time are the three factors that govern the population dynamics. Typically, greater band gap, smaller NA coupling, and faster pure-dephasing lead to longer recombination. The band gap is smaller for the edge system, even though the recombination is slower. Therefore, the slower recombination is rationalized by the smaller NA coupling and faster pure-dephasing (Table 2). The NA coupling is smaller in the edge system, because of the decreased overlap of electron and hole wave functions that are typically localized on the opposite sides (Figures 3, S1, and S2). The pure-dephasing is faster because the separated electrons and holes are less correlated, and because the edge state couple to a broader range of vibrational modes (Figure 5). The simulation cell allows only for a modest electron−hole

https://dx.doi.org/10.1021/acs.jpclett.0c02800
J. Phys. Chem. Lett. 2020, 11, 9100−9109

separation. Nevertheless, the carrier lifetime is nearly 3 times longer in the presence of the edges. In realistic systems with a much better charge separation, the enhancement in the carrier lifetime is more significant. The model used in the present study captures the properties of the edges and explains in detail the mechanism underlying the experimentally observed increase in the carrier lifetimes. The study identifies the factors that govern the nonradiative electron−hole recombination and demonstrates how these factors are influenced by the edges. The analysis is performed from a fully atomistic perspective and explicitly in the time-domain, most closely mimicking the time-resolved experiments.

To summarize, we have investigated nonradiative electron−hole recombination in the $MAPbBr_3$ perovskite with and without edges, using a combination of NAMD and *ab initio* real-time TDDFT. The simulations show that unsaturated chemical bonds at $MAPbBr_3$ nanostructure edges do not create deep trap states for electrons and holes. Instead, the edge states are characterized by a continuous distribution of energies within about 0.1 eV of conduction and valence bands. Further, the edge states are coupled strongly to the band states and mix with them. As a result, edges of $MAPbBr_3$ nanostructures provide a driving force for separation of photo-generated excitons into free electrons and holes, which remain mobile and can carry electrical current. The spatial separation of electrons and holes minimizes overlap of their wave functions and decreases the NA coupling responsible for the nonradiative carrier losses. The increased mobility of edge atoms and lowering of the structural symmetry at the edges activate additional vibrational motions that accelerate elastic charge−phonon scattering, inducing coherence loss within the electronic subsystem and slowing down quantum dynamics of carrier recombination. The majority of the electron−phonon coupling arises from slow motions of the Pb−Br inorganic lattice with frequencies around 100 cm^{-1}. Faster motions of the organic MA cations with frequencies up to 300 cm^{-1} contribute strongly at the edges. Large amplitude motions of edge atoms induce fluctuations of edge-state energies, facilitating energy crossings and coupling of edge and bulk wave functions. The decreased NA coupling and shortened coherence time extend charge carrier lifetimes by a factor of 3 in the edge system relative to the pristine structure. Observed already in the simulation cell, the lifetime enhancement should be much more significant in real systems allowing for long-range edge-driven separation of electrons and holes. Edges of perovskite microstructures facilitate exciton dissociation into free charges, slow down nonradiative electron−hole recombination, while at the same time, do not create deep trap states and maintain charges mobility. All of these factors improve performance of photovoltaic and optoelectronic devices. Our study establishes the atomistic mechanism responsible for long-lived charge carriers in the edge areas of the $MAPbBr_3$ perovskite, provides a detailed understanding of the complex relationships between local structural morphology and the material's photo-physical properties, and generates valuable insights for design and optimization of advanced perovskite materials and devices.

■ ASSOCIATED CONTENT

Supporting Information

The Supporting Information is available free of charge at https://pubs.acs.org/doi/10.1021/acs.jpclett.0c02800.

Charge densities of edge states in symmetric $MAPbBr_3$ structures with nonstoichiometric MAI- and PbI_2-terminated edges and charge densities of edge states with randomly rotated MA cations (PDF)

■ AUTHOR INFORMATION

Corresponding Author

Run Long − *College of Chemistry, Key Laboratory of Theoretical & Computational Photochemistry of Ministry of Education, Beijing Normal University, Beijing 100875, People's Republic of China;* orcid.org/0000-0003-3912-8899; Email: runlong@bnu.edu.cn

Authors

Ran Shi − *College of Chemistry, Key Laboratory of Theoretical & Computational Photochemistry of Ministry of Education, Beijing Normal University, Beijing 100875, People's Republic of China*

Andrey S. Vasenko − *National Research University Higher School of Economics, 101000 Moscow, Russia; I.E. Tamm Department of Theoretical Physics, P.N. Lebedev Physical Institute, Russian Academy of Sciences, 119991 Moscow, Russia;* orcid.org/0000-0002-2978-8650

Oleg V. Prezhdo − *Departments of Chemistry, and Physics and Astronomy, University of Southern California, Los Angeles, California 90089, United States;* orcid.org/0000-0002-5140-7500

Complete contact information is available at: https://pubs.acs.org/10.1021/acs.jpclett.0c02800

Notes

The authors declare no competing financial interest.

■ ACKNOWLEDGMENTS

R.S. and R.L. acknowledge support of the National Science Foundation of China, Grant Nos. 21573022, 21973006, and 51861135101. R.L. acknowledges the Recruitment Program of Global Youth Experts of China and the Beijing Normal University Startup. O.V.P. acknowledges support of the U.S. National Science Foundation, Grant No. CHE-1900510.

■ REFERENCES

(1) Kojima, A.; Teshima, K.; Shirai, Y.; Miyasaka, T. Organometal Halide Perovskites as Visible-Light Sensitizers for Photovoltaic Cells. *J. Am. Chem. Soc.* **2009**, *131*, 6050−6051.

(2) National Renewable Energy Laboratory (NREL). *Best Research Cell Efficiency Chart*, https://www.nrel.gov/pv/cell-efficiency.html (accessed 2020-09-13).

(3) Calvo, M. E. Materials Chemistry Approaches to the Control of the Optical Features of Perovskite Solar Cells. *J. Mater. Chem. A* **2017**, *5*, 20561−20578.

(4) Saparov, B.; Mitzi, D. B. Organic-Inorganic Perovskites: Structural Versatility for Functional Materials Design. *Chem. Rev.* **2016**, *116*, 4558−4596.

(5) Shi, D.; Adinolfi, V.; Comin, R.; Yuan, M.; Alarousu, E.; Buin, A.; Chen, Y.; Hoogland, S.; Rothenberger, A.; Katsiev, K.; et al. Low Trap-State Density and Long Carrier Diffusion in Organolead Trihalide Perovskite Single Crystals. *Science* **2015**, *347*, 519−522.

(6) Yin, W.-J.; Yang, J.-H.; Kang, J.; Yan, Y.; Wei, S.-H. Halide Perovskite Materials for Solar Cells: A Theoretical Review. *J. Mater. Chem. A* **2015**, *3*, 8926−8942.

(7) Meggiolaro, D.; Motti, S. G.; Mosconi, E.; Barker, A. J.; Ball, J.; Perini, C. A. R.; Deschler, F.; Petrozza, A.; De Angelis, F. Iodine

Chemistry Determines the Defect Tolerance of Lead-Halide Perovskites. *Energy Environ. Sci.* **2018**, *11*, 702−713.
(8) Pellet, N.; Gao, P.; Gregori, G.; Yang, T.-Y.; Nazeeruddin, M. K.; Maier, J.; Graetzel, M. Mixed-Organic-Cation Perovskite Photovoltaics for Enhanced Solar-Light Harvesting. *Angew. Chem., Int. Ed.* **2014**, *53*, 3151−3157.
(9) Ju, D.; Dang, Y.; Zhu, Z.; Liu, H.; Chueh, C.-C.; Li, X.; Wang, L.; Hu, X.; Jen, A. K. Y.; Tao, X. Tunable Band Gap and Long Carrier Recombination Lifetime of Stable Mixed $CH_3NH_3Pb_xSn_{1-X}Br_3$ Single Crystals. *Chem. Mater.* **2018**, *30*, 1556−1565.
(10) Turren-Cruz, S.-H.; Saliba, M.; Mayer, M. T.; Juarez-Santiesteban, H.; Mathew, X.; Nienhaus, L.; Tress, W.; Erodici, M. P.; Sher, M.-J.; Bawendi, M. G.; et al. Enhanced Charge Carrier Mobility and Lifetime Suppress Hysteresis and Improve Efficiency in Planar Perovskite Solar Cells. *Energy Environ. Sci.* **2018**, *11*, 78−86.
(11) Ball, J. M.; Lee, M. M.; Hey, A.; Snaith, H. J. Low-Temperature Processed Meso-Superstructured to Thin-Film Perovskite Solar Cells. *Energy Environ. Sci.* **2013**, *6*, 1739−1743.
(12) Green, M. A.; Ho-Baillie, A.; Snaith, H. J. The Emergence of Perovskite Solar Cells. *Nat. Photonics* **2014**, *8*, 506−514.
(13) Xing, G.; Mathews, N.; Lim, S. S.; Yantara, N.; Liu, X.; Sabba, D.; Gratzel, M.; Mhaisalkar, S.; Sum, T. C. Low-Temperature Solution-Processed Wavelength-Tunable Perovskites for Lasing. *Nat. Mater.* **2014**, *13*, 476−480.
(14) Wu, Y.; Li, J.; Xu, J.; Du, Y.; Huang, L.; Ni, J.; Cai, H.; Zhang, J. Organic-Inorganic Hybrid $CH_3NH_3PbI_3$ Perovskite Materials as Channels in Thin-Film Field-Effect Transistors. *RSC Adv.* **2016**, *6*, 16243−16249.
(15) Cao, F.; Meng, L.; Wang, M.; Tian, W.; Li, L. Gradient Energy Band Driven High-Performance Self-Powered Perovskite/CdS Photodetector. *Adv. Mater.* **2019**, *31*, 1806725.
(16) Wei, Z.; Xing, J. The Rise of Perovskite Light-Emitting Diodes. *J. Phys. Chem. Lett.* **2019**, *10*, 3035−3042.
(17) deQuilettes, D. W.; Vorpahl, S. M.; Stranks, S. D.; Nagaoka, H.; Eperon, G. E.; Ziffer, M. E.; Snaith, H. J.; Ginger, D. S. Impact of Microstructure on Local Carrier Lifetime in Perovskite Solar Cells. *Science* **2015**, *348*, 683−686.
(18) Grancini, G.; Viola, D.; Gandini, M.; Altamura, D.; Pogna, E. A. A.; D'Innocenzo, V.; Bargigia, I.; Giannini, C.; Cerullo, G.; Petrozza, A. Lattice Distortions Drive Electron-Hole Correlation within Micrometer-Size Lead-Iodide Perovskite Crystals. *ACS Energy Lett.* **2017**, *2*, 265−269.
(19) Ciesielski, R.; Schafer, F.; Hartmann, N. F.; Giesbrecht, N.; Bein, T.; Docampo, P.; Hartschuh, A. Grain Boundaries Act as Solid Walls for Charge Carrier Diffusion in Large Crystal MAPI Thin Films. *ACS Appl. Mater. Interfaces* **2018**, *10*, 7974−7981.
(20) Grancini, G.; D'Innocenzo, V.; Dohner, E. R.; Martino, N.; Kandada, A. R. S.; Mosconi, E.; De Angelis, F.; Karunadasa, H. I.; Hoke, E. T.; Petrozza, A. $CH_3NH_3PbI_3$ Perovskite Single Crystals: Surface Photophysics and Their Interaction with the Environment. *Chem. Sci.* **2015**, *6*, 7305−7310.
(21) Hill, A. H.; Smyser, K. E.; Kennedy, C. L.; Massaro, E. S.; Grumstrup, E. M. Screened Charge Carrier Transport in Methylammonium Lead Iodide Perovskite Thin Films. *J. Phys. Chem. Lett.* **2017**, *8*, 948−953.
(22) Prezhdo, O. V. Multiple Excitons and the Electron-Phonon Bottleneck in Semiconductor Quantum Dots: An Ab Initio Perspective. *Chem. Phys. Lett.* **2008**, *460*, 1−9.
(23) Kanemitsu, Y. Trion Dynamics in Lead Halide Perovskite Nanocrystals. *J. Chem. Phys.* **2019**, *151*, 170902.
(24) Chen, T. R.; Chen, W. L.; Foley, B. J.; Lee, J.; Ruff, J. P. C.; Ko, J. Y. P.; Brown, C. M.; Harriger, L. W.; Zhang, D. P.; Park, C. W.; et al. Origin of Long Lifetime of Band-Edge Charge Carriers in Organic-Inorganic Lead Iodide Perovskites. *Proc. Natl. Acad. Sci. U. S. A.* **2017**, *114*, 7519−7524.
(25) Nah, S.; Spokoyny, B. M.; Soe, C. M. M.; Stoumpos, C. C.; Kanatzidis, M. G.; Harel, E. Ultrafast Imaging of Carrier Cooling in Metal Halide Perovskite Thin Films. *Nano Lett.* **2018**, *18*, 1044−1048.
(26) Zhang, Z. Y.; Yu, K.; Wang, G. P. Edge Effect on the Population of Free Carriers and Excitons in Single-Crystal $CH_3NH_3PbBr_3$ Perovskite Nanomaterials. *Adv. Electron. Mater.* **2019**, *5*, 1900216.
(27) Simpson, M. J.; Doughty, B.; Yang, B.; Xiao, K.; Ma, Y. Z. Spatial Localization of Excitons and Charge Carriers in Hybrid Perovskite Thin Films. *J. Phys. Chem. Lett.* **2015**, *6*, 3041−3047.
(28) Grancini, G.; Kandada, A. R. S.; Frost, J. M.; Barker, A. J.; De Bastiani, M.; Gandini, M.; Marras, S.; Lanzani, G.; Walsh, A.; Petrozza, A. Role of Microstructure in the Electron-Hole Interaction of Hybrid Lead Halide Perovskites. *Nat. Photonics* **2015**, *9*, 695−701.
(29) Shi, E. Z.; Deng, S. B.; Yuan, B.; Gao, Y.; Akriti; Yuan, L.; Davis, C. S.; Zemlyanov, D.; Yu, Y.; Huang, L. B.; et al. Extrinsic and Dynamic Edge States of Two-Dimensional Lead Halide Perovskites. *ACS Nano* **2019**, *13*, 1635−1644.
(30) Blancon, J. C.; Tsai, H.; Nie, W.; Stoumpos, C. C.; Pedesseau, L.; Katan, C.; Kepenekian, M.; Soe, C. M. M.; Appavoo, K.; Sfeir, M. Y.; et al. Extremely Efficient Internal Exciton Dissociation through Edge States in Layered 2D Perovskites. *Science* **2017**, *355*, 1288−1291.
(31) Zhang, Z.; Fang, W.-H.; Long, R.; Prezhdo, O. V. Exciton Dissociation and Suppressed Charge Recombination at 2D Perovskite Edges: Key Roles of Unsaturated Halide Bonds and Thermal Disorder. *J. Am. Chem. Soc.* **2019**, *141*, 15557−15566.
(32) Kepenekian, M.; Traore, B.; Blancon, J. C.; Pedesseau, L.; Tsai, H.; Nie, W. Y.; Stoumpos, C. C.; Kanatzidis, M. G.; Even, J.; Mohite, A. D.; et al. Concept of Lattice Mismatch and Emergence of Surface States in Two-Dimensional Hybrid Perovskite Quantum Wells. *Nano Lett.* **2018**, *18*, 5603−5609.
(33) Runge, E.; Gross, E. K. U. Density-Functional Theory for Time-Dependent Systems. *Phys. Rev. Lett.* **1984**, *52*, 997−1000.
(34) Akimov, A. V.; Prezhdo, O. V. Advanced Capabilities of the Pyxaid Program: Integration Schemes, Decoherenc:E Effects, Multiexcitonic States, and Field-Matter Interaction. *J. Chem. Theory Comput.* **2014**, *10*, 789−804.
(35) Akimov, A. V.; Prezhdo, O. V. The Pyxaid Program for Non-Adiabatic Molecular Dynamics in Condensed Matter Systems. *J. Chem. Theory Comput.* **2013**, *9*, 4959−4972.
(36) Craig, C. F.; Duncan, W. R.; Prezhdo, O. V. Trajectory Surface Hopping in the Time-Dependent Kohn-Sham Approach for Electron-Nuclear Dynamics. *Phys. Rev. Lett.* **2005**, *95*, 163001−163005.
(37) Jaeger, H. M.; Fischer, S.; Prezhdo, O. V. Decoherence-Induced Surface Hopping. *J. Chem. Phys.* **2012**, *137*, 22A545.
(38) Kohn, W.; Sham, L. J. Self-Consistent Equations Including Exchange and Correlation Effects. *Phys. Rev.* **1965**, *140*, A1133−A1139.
(39) Fischer, S. A.; Habenicht, B. F.; Madrid, A. B.; Duncan, W. R.; Prezhdo, O. V. Regarding the Validity of the Time-Dependent Kohn−Sham Approach for Electron-Nuclear Dynamics Via Trajectory Surface Hopping. *J. Chem. Phys.* **2011**, *134*, 024102.
(40) Akimov, A. V.; Long, R.; Prezhdo, O. V. Coherence Penalty Functional: A Simple Method for Adding Decoherence in Ehrenfest Dynamics. *J. Chem. Phys.* **2014**, *140*, 194107.
(41) Mukamel, S. *Principles of Nonlinear Optical Spectroscopy*; Oxford University Press: New York, 1995.
(42) Misra, B.; Sudarshan, E. C. G. Zenos Paradox in Quantum Theory. *J. Math. Phys.* **1977**, *18*, 756−763.
(43) Prezhdo, O. V. Quantum Anti-Zeno Acceleration of a Chemical Reaction. *Phys. Rev. Lett.* **2000**, *85*, 4413−4417.
(44) Wang, Y. T.; Fang, W. H.; Long, R.; Prezhdo, O. V. Symmetry Breaking at $MAPbI_3$ Perovskite Grain Boundaries Suppresses Charge Recombination: Time-Domain Ab Initio Analysis. *J. Phys. Chem. Lett.* **2019**, *10*, 1617−1623.
(45) Zhang, Z.; Long, R. Doping-Induced Rapid Decoherence Suppresses Charge Recombination in Mono/Divalent Cations Mixed Perovskite from Nonadiabatic Molecular Dynamics Simulation. *J. Phys. Chem. Lett.* **2019**, *10*, 3433−3439.
(46) Qiao, L.; Fang, W.-H.; Long, R.; Prezhdo, O. V. Extending Carrier Lifetimes in Lead Halide Perovskites with Alkali Metals by

https://dx.doi.org/10.1021/acs.jpclett.0c02800
J. Phys. Chem. Lett. 2020, 11, 9100−9109

Passivating and Eliminating Halide Interstitial Defects. *Angew. Chem., Int. Ed.* **2020**, *59*, 4684.
(47) Zhang, Z. S.; Fang, W. H.; Tokina, M. V.; Long, R.; Prezhdo, O. V. Rapid Decoherence Suppresses Charge Recombination in Multi-Layer 2D Halide Perovskites: Time-Domain Ab Initio Analysis. *Nano Lett.* **2018**, *18*, 2459−2466.
(48) Shi, R.; Zhang, Z.; Fang, W.-H.; Long, R. Charge Localization Control of Electron-Hole Recombination in Multilayer Two-Dimensional Dion-Jacobson Hybrid Perovskites. *J. Mater. Chem. A* **2020**, *8*, 9168−9176.
(49) Long, R.; Prezhdo, O. V. Dopants Control Electron-Hole Recombination at Perovskite-TiO_2 Interfaces: Ab Initio Time-Domain Study. *ACS Nano* **2015**, *9*, 11143−11155.
(50) Hyeon-Deuk, K.; Prezhdo, O. V. Multiple Exciton Generation and Recombination Dynamics in Small Si and CdSe Quantum Dots: An Ab Initio Time-Domain Study. *ACS Nano* **2012**, *6*, 1239−1250.
(51) Chaban, V. V.; Prezhdo, V. V.; Prezhdo, O. V. Covalent Linking Greatly Enhances Photoinduced Electron Transfer in Fullerene-Quantum Dot Nanocomposites: Time-Domain Ab Initio Study. *J. Phys. Chem. Lett.* **2013**, *4*, 1−6.
(52) Long, R.; Prezhdo, O. V. Instantaneous Generation of Charge-Separated State on TiO_2 Surface Sensitized with Plasmonic Nanoparticles. *J. Am. Chem. Soc.* **2014**, *136*, 4343−4354.
(53) Zhang, Z. S.; Liu, L. H.; Fang, W. H.; Long, R.; Tokina, M. V.; Prezhdo, O. V. Plasmon-Mediated Electron Injection from Au Nanorods into MoS2: Traditional Versus Photoexcitation Mechanism. *Chem.* **2018**, *4*, 1112−1127.
(54) Wei, Y.; Long, R. Grain Boundaries Are Benign and Suppress Nonradiative Electron-Hole Recombination in Monolayer Black Phosphorus: A Time-Domain Ab Initio Study. *J. Phys. Chem. Lett.* **2018**, *9*, 3856−3862.
(55) Zhang, L. L.; Vasenko, A. S.; Zhao, J.; Prezhdo, O. V. Mono-Elemental Properties of 2D Black Phosphorus Ensure Extended Charge Carrier Lifetimes under Oxidation: Time-Domain Ab Initio Analysis. *J. Phys. Chem. Lett.* **2019**, *10*, 1083.
(56) Akimov, A. V.; Asahi, R.; Jinnouchi, R.; Prezhdo, O. V. What Makes the Photocatalytic CO_2 Reduction on N-Doped Ta_2O_5 Efficient: Insights from Nonadiabatic Molecular Dynamics. *J. Am. Chem. Soc.* **2015**, *137*, 11517−11525.
(57) Chaban, V. V.; Prezhdo, V. V.; Prezhdo, O. V. Covalent Linking Greatly Enhances Photoinduced Electron Transfer in Fullerene-Quantum Dot Nanocomposites: Time-Domain Ab Initio Study. *J. Phys. Chem. Lett.* **2013**, *4*, 1−6.
(58) He, J. L.; Casanova, D.; Fang, W. H.; Long, R.; Prezhdo, O. V. Mai Termination Favors Efficient Hole Extraction and Slow Charge Recombination at the $MAPbI_3$/CuSCN Heterojunction. *J. Phys. Chem. Lett.* **2020**, *11*, 4481−4489.
(59) He, J. L.; Vasenko, A. S.; Long, R.; Prezhdo, O. V. Halide Composition Controls Electron-Hole Recombination in Cesium-Lead Halide Perovskite Quantum Dots: A Time Domain Ab Lnitio Study. *J. Phys. Chem. Lett.* **2018**, *9*, 1872−1879.
(60) Li, W.; Chen, Z.; Tang, J. F.; Prezhdo, O. V. Anti-Correlation between Band Gap and Carrier Lifetime in Lead Halide Perovskites under Compression Rationalized by Ab Initio Quantum Dynamics. *Chem. Mater.* **2020**, *32*, 4707−4715.
(61) Stier, W.; Duncan, W. R.; Prezhdo, O. V. Thermally Assisted Sub-10 Fs Electron Transfer in Dye-Sensitized Nanocrystalline TiO2 Solar Cells. *Adv. Mater.* **2004**, *16*, 240.
(62) Long, R.; Casanova, D.; Fang, W. H.; Prezhdo, O. V. Donor Acceptor Interaction Determines the Mechanism of Photoinduced Electron Injection from Graphene Quantum Dots into TiO2:Pi-Stacking Supersedes Covalent Bonding. *J. Am. Chem. Soc.* **2017**, *139*, 2619−2629.
(63) Long, R.; English, N. J.; Prezhdo, O. V. Minimizing Electron−Hole Recombination on TiO2 Sensitized with PbSe Quantum Dots: Time-Domain Ab Initio Analysis. *J. Phys. Chem. Lett.* **2014**, *5*, 2941−2946.
(64) Kresse, G.; Furthmuller, J. Efficient Iterative Schemes for Ab Initio Total-Energy Calculations Using a Plane-Wave Basis Set. *Phys. Rev. B: Condens. Matter Mater. Phys.* **1996**, *54*, 11169−11186.
(65) Perdew, J. P.; Burke, K.; Ernzerhof, M. Generalized Gradient Approximation Made Simple. *Phys. Rev. Lett.* **1996**, *77*, 3865−3868.
(66) Blöchl, P. E. Projector Augmented-Wave Method. *Phys. Rev. B: Condens. Matter Mater. Phys.* **1994**, *50*, 17953−17979.
(67) Monkhorst, H. J.; Pack, J. D. Special Points for Brillouin-Zone Integrations. *Phys. Rev. B* **1976**, *13*, 5188−5192.
(68) Grimme, S.; Antony, J.; Ehrlich, S.; Krieg, H. A Consistent and Accurate Ab Initio Parametrization of Density Functional Dispersion Correction (DFT−D) for the 94 Elements H-Pu. *J. Chem. Phys.* **2010**, *132*, 154104−154124.
(69) Grimme, S.; Ehrlich, S.; Goerigk, L. Effect of the Damping Function in Dispersion Corrected Density Functional Theory. *J. Comput. Chem.* **2011**, *32*, 1456−1465.
(70) Meng, R.; Wu, G.; Zhou, J.; Zhou, H.; Fang, H.; Loi, M. A.; Zhang, Y. Understanding the Impact of Bismuth Heterovalent Doping on the Structural and Photophysical Properties of $CH_3NH_3PbBr_3$ Halide Perovskite Crystals with near-Ir Photoluminescence. *Chem. - Eur. J.* **2019**, *25*, 5480−5488.
(71) Nayak, P. K.; Sendner, M.; Wenger, B.; Wang, Z.; Sharma, K.; Ramadan, A. J.; Lovrincic, R.; Pucci, A.; Madhu, P. K.; Snaith, H. J. Impact of Bi^{3+} Heterovalent Doping in Organic-Inorganic Metal Halide Perovskite Crystals. *J. Am. Chem. Soc.* **2018**, *140*, 574−577.
(72) Rakita, Y.; Cohen, S. R.; Kedem, N. K.; Hodes, G.; Cahen, D. Mechanical Properties of $APbX_3$ (a = Cs or CH_3NH_3; X = I or Br) Perovskite Single Crystals. *MRS Commun.* **2015**, *5*, 623−629.
(73) Li, J.-L.; Yang, J.; Wu, T.; Wei, S.-H. Formation of Dy Center as N-Type Limiting Defects in Octahedral Semiconductors: The Case of Bi-Doped Hybrid Halide Perovskites. *J. Mater. Chem. C* **2019**, *7*, 4230−4234.
(74) Kitazawa, N.; Watanabe, Y.; Nakamura, Y. Optical Properties of $CH_3NH_3PbX_3$ (X = Halogen) and Their Mixed-Halide Crystals. *J. Mater. Sci.* **2002**, *37*, 3585−3587.
(75) Yin, W.-J.; Yan, Y.; Wei, S.-H. Anomalous Alloy Properties in Mixed Halide Perovskites. *J. Phys. Chem. Lett.* **2014**, *5*, 3625−3631.
(76) Juarez-Perez, E. J.; Sanchez, R. S.; Badia, L.; Garcia-Belmonte, G.; Kang, Y. S.; Mora-Sero, I.; Bisquert, J. Photoinduced Giant Dielectric Constant in Lead Halide Perovskite Solar Cells. *J. Phys. Chem. Lett.* **2014**, *5*, 2390−2394.
(77) Justo, J. F.; de Brito Mota, F.; Fazzio, A. First-Principles Investigation of a-Sinx: H. *Phys. Rev. B: Condens. Matter Mater. Phys.* **2002**, *65*, 073202.
(78) Ashhab, S.; Voznyy, O.; Hoogland, S.; Sargent, E. H.; Madjet, M. E. Effect of Disorder on Transport Properties in a Tight-Binding Model for Lead Halide Perovskites. *Sci. Rep.* **2017**, *7*, 8902.
(79) Sowers, K. L.; Hou, Z. T.; Peterson, J. J.; Swartz, B.; Pal, S.; Prezhdo, O.; Krauss, T. D. Photophysical Properties of CsSe/CdS Core/Shell Quantum Dots with Tunable Surface Composition. *Chem. Phys.* **2016**, *471*, 24−31.
(80) Wei, H. H. Y.; Evans, C. M.; Swartz, B. D.; Neukirch, A. J.; Young, J.; Prezhdo, O. V.; Krauss, T. D. Colloidal Semiconductor Quantum Dots with Tunable Surface Composition. *Nano Lett.* **2012**, *12*, 4465−4471.
(81) Kilina, S. V.; Neukirch, A. J.; Habenicht, B. F.; Kilin, D. S.; Prezhdo, O. V. Quantum Zeno Effect Rationalizes the Phonon Bottleneck in Semiconductor Quantum Dots. *Phys. Rev. Lett.* **2013**, *110*, 180404.
(82) Xie, L.-Q.; Zhang, T.-Y.; Chen, L.; Guo, N.; Wang, Y.; Liu, G.-K.; Wang, J.-R.; Zhou, J.-Z.; Yan, J.-W.; Zhao, Y.-X.; et al. Organic-Inorganic Interactions of Single Crystalline Organolead Halide Perovskites Studied by Raman Spectroscopy. *Phys. Chem. Chem. Phys.* **2016**, *18*, 18112−18118.
(83) Leguy, A. M. A.; Goni, A. R.; Frost, J. M.; Skelton, J.; Brivio, F.; Rodriguez-Martinez, X.; Weber, O. J.; Pallipurath, A.; Isabel Alonso, M.; Campoy-Quiles, M.; et al. Dynamic Disorder, Phonon Lifetimes, and the Assignment of Modes to the Vibrational Spectra of

https://dx.doi.org/10.1021/acs.jpclett.0c02800
J. Phys. Chem. Lett. 2020, 11, 9100−9109

Methylammonium Lead Halide Perovskites. *Phys. Chem. Chem. Phys.* **2016**, *18*, 27051−27066.
(84) Ledinsky, M.; Loeper, P.; Niesen, B.; Holovsky, J.; Moon, S.-J.; Yum, J.-H.; De Wolf, S.; Fejfar, A.; Ballif, C. Raman Spectroscopy of Organic-Inorganic Halide Perovskites. *J. Phys. Chem. Lett.* **2015**, *6*, 401−406.
(85) Quarti, C.; Grancini, G.; Mosconi, E.; Bruno, P.; Ball, J. M.; Lee, M. M.; Snaith, H. J.; Petrozza, A.; De Angelis, F. The Raman Spectrum of the $CH_3NH_3PbI_3$ Hybrid Perovskite: Interplay of Theory and Experiment. *J. Phys. Chem. Lett.* **2014**, *5*, 279−284.
(86) Li, W.; Vasenko, A. S.; Tang, J. F.; Prezhdo, O. V. Anharmonicity Extends Carrier Lifetimes in Lead Halide Perovskites at Elevated Temperatures. *J. Phys. Chem. Lett.* **2019**, *10*, 6219−6226.
(87) Akimov, A. V.; Prezhdo, O. V. Persistent Electronic Coherence Despite Rapid Loss of Electron-Nuclear Correlation. *J. Phys. Chem. Lett.* **2013**, *4*, 3857−3864.
(88) Yamada, T.; Yamada, Y.; Nishimura, H.; Nakaike, Y.; Wakamiya, A.; Murata, Y.; Kanemitsu, Y. Fast Free-Carrier Diffusion in $CH_3NH_3PbBr_3$ Single Crystals Revealed by Time-Resolved One- and Two-Photon Excitation Photoluminescence Spectroscopy. *Adv. Electron. Mater.* **2016**, *2*, 1500290.
(89) Wang, K. H.; Li, L. C.; Shellaiah, M.; Sun, K. W. Structural and Photophysical Properties of Methylammonium Lead Tribromide ($MAPbBr_3$) Single Crystals. *Sci. Rep.* **2017**, *7*, 13643.

https://dx.doi.org/10.1021/acs.jpclett.0c02800
J. Phys. Chem. Lett. 2020, 11, 9100−9109